Published in IET Optoelectronics
Received on 29th August 2014
Revised on 29th October 2014
Accepted on 14th November 2014
doi: 10.1049/iet-opt.2014.0093

Special Issue on selected papers from the Semiconductor and Integrated OptoElectronics Conference 2014

ISSN 1751-8768

Manufacturing-tolerant compact red-emitting laser diode designs for next generation applications

Stella Nina Elliott, Peter M. Smowton

School of Physics and Astronomy, Cardiff University, Queens Buildings, The Parade, Cardiff, CF24 3AA, UK
E-mail: ElliottS1@Cardiff.ac.uk

Abstract: Quantum well laser diodes with low far-field divergence remain a requirement for many applications such as optical interconnects and data networks, pump sources and next generation holographic red–green–blue displays requiring compact, high power, visible light sources with high spatial and spectral coherence. Many designs exist, but the structure must be easy to grow reproducibly, which has commercial advantages. The authors' low far-field divergence design widens the vertical mode in such a way as to decrease the far-field divergence without significantly reducing the confinement factor, thus keeping threshold current lower. In this study, the authors calculate the sensitivity of their design, which has high refractive index mode expansion layers inserted in the cladding, to unintentional variations in layer thickness and composition during growth. They obtain consistency in measured far-fields for three wafers grown over an interval of a year, with a full-width-half-maximum vertical far-field divergence of 17° for a narrow design (Design A) and just under 13° for a very narrow design (Design B). They have demonstrated a useful, reproducible design, adding to the range of versatile semiconductor lasers available for every application.

1 Introduction

Quantum well laser diodes with low far-field divergence remain a topic of concentrated research and development effort with applications such as optical interconnects and data networks, pump sources [1] and next generation holographic red–green–blue displays requiring compact, high power, visible light sources with high spatial and spectral coherence [2]. Many types of designs for lasers with narrow vertical far-fields have been investigated, including large and super large optical cavity ([S]LOC) [3], photonic bandgap crystal (PBC) structures [4] and designs with extra layers in the optical waveguide [5–8]. Good control of the far-field divergence is achieved in all these designs, with vertical divergence reduced from a typical 35° or more in earlier designs, to 8–18° in structures designed for control of the vertical far-field. In this way the astigmatism of the beam is reduced, enabling structures such as these to be used without expensive beam shaping optics when a round spot is required, but greater power is required than can be provided by vertical cavity surface-emitting lasers. One advantage of designs with extra waveguide layers over LOC or PBC is that they are thinner and not only generate less heat, but dissipate it more easily. In addition, growth is simpler with a smaller number of epitaxial layers. The sensitivity of the optical mode to precise waveguide layer thicknesses and compositions varies with design and may lead to more exacting growth requirements in manufacture. A structure that is easy to grow reproducibly has commercial advantages. In this paper, we calculate the sensitivity of our design to variations in layer thickness and composition during growth, selecting designs with lowest sensitivity and obtaining repeated growths which show excellent reproducibility. These are structures with extra high refractive index layers (mode expansion (ME) layers) inserted in the low index cladding layers. This widens the vertical mode in such a way as to decrease the far-field divergence without significantly reducing the confinement factor, a problem in some designs as it leads to increased threshold current density. We included ME layers in both p and n cladding layers of our realised structures, as this reduces the rate at which the mode changes with layer thickness or composition compared with a layer inserted on the n-side only. We have previously grown lasers with a vertical far-field divergence of 18°. In this paper, we designate this as Design A. Full details are given of the structure in [6] and the waveguide is described below. We now consider the sensitivity of our design to unintended variations in cladding layer thickness and composition during growth. We show the existence of regions in the design space where a small change in design parameter has relatively little effect on the mode width, and thus is less sensitive to variations in growth conditions during manufacture. We present far-field measurements on a series of growths of Design A to confirm the manufacturing reproducibility. We also report on a new structure with a narrower measured vertical far-field divergence of <13° (Design B).

2 Design of waveguide structure

In this paper, we consider 650 nm band emitting GaInP quantum well structures in an AlGaInP waveguide lattice

matched to and grown by metal oxide chemical vapour deposition (MOCVD) on GaAs. The active region consists of three 5 nm wide, compressively strained $Ga_{0.48}In_{0.52}P$ quantum wells separated by 5.5 nm $(Al_{0.5}Ga_{0.5})_{0.52}In_{0.48}P$ barriers, centrally placed in the $(Al_{0.5}Ga_{0.5})_{0.52}In_{0.48}P$ core of total width 0.226 μm which supports a single transverse optical mode. (The structure could easily be adapted for 630 nm emission with tensile strained quantum wells and a slightly narrower core [9].) The waveguide consists of this high refractive index core, placed in low refractive index $(Al_{0.7}Ga_{0.3})_{0.52}In_{0.48}P$ cladding (Fig. 1).

Two $(Al_{0.5}Ga_{0.5})_{0.52}In_{0.48}P$ ME layers, of the same refractive index as the core, are inserted symmetrically in the $(Al_{0.7}Ga_{0.3})_{0.52}In_{0.48}P$ waveguide cladding. Grown wafers Design A and Design B both have this schematic structure: increasing the spacing and width of the ME layers narrows the far-field, going from A to B. An asymmetric design with an ME layer in the n-cladding only was also modelled, but not grown. The active region consists of three quantum wells centrally placed in the $(Al_{0.5}Ga_{0.5})_{0.52}In_{0.48}P$ waveguide core.

The design feature that narrows the far-field is the insertion of $(Al_{0.5}Ga_{0.5})_{0.52}In_{0.48}P$ high refractive index ME layers in the $(Al_{0.7}Ga_{0.3})_{0.52}In_{0.48}P$ cladding. An ME layer pulls the mode out into a small side lobe, producing a wider near-field and correspondingly narrower far-field, whereas the electric field amplitude and intensity at the centre of the mode, where the overlap with the quantum wells is greatest, remain high, with concomitantly lower threshold.

We modelled symmetric designs, with ME layers in both p- and n-claddings, and asymmetric designs with an ME layer placed in the n-cladding only. The symmetric design has advantages such as a reduced sensitivity to manufacturing variations, but in some cases there is a requirement for not increasing the mode confinement in the p-doped cladding with associated increase in free carrier absorption losses, in which case an asymmetric design could be used. We modelled the effect of changing the width and spacing (Fig. 1) of the ME layers, keeping the core and active region the same throughout the modelling process. We selected a symmetric design for growth.

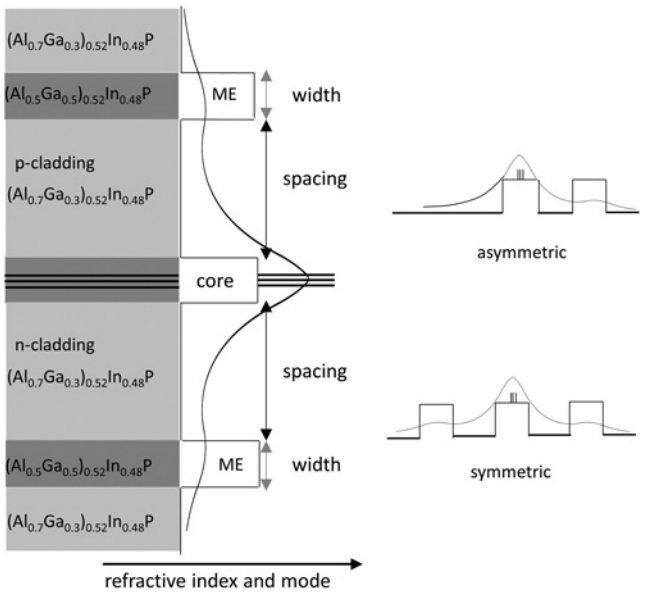

Fig. 1 *Schema of the narrow vertical far-field designs considered in this paper*

We modelled the structures using the transfer matrix method in a one-dimensional (1D) slab waveguide to calculate the electric field amplitude and near-field intensity of the optical mode as a function of distance across the structure for a specific wavelength (650 nm in the first instance), performing a Fourier transform to obtain far-field as a function of angle. The input data consisted of layer thicknesses (with the cladding layer considered effectively infinitely wide), real refractive indices of these layers and the lasing wavelength. The output data consisted of far-field as a function of angle and the confinement factor for each layer, defined as the fraction of the near-field intensity spatially confined in that epitaxial layer.

The room temperature refractive indices of the AlGaInP waveguide layers were calculated using the modified single electron oscillator model. On the basis of the semi-empirical single electron oscillator method of Wemple and DiDomenico [10], this model was developed by Afromowitz [11] for AlGaAs to obtain a better fit to experimentally obtained refractive index values near the band edge and extended to AlGaInP by Kaneko and Kishino [12], giving the following relations used in this paper

$$n^2 - 1 = \frac{E_d}{E_o} + \frac{(\hbar\omega)^2 E_d}{E_o^3} + \frac{(\hbar\omega)^4 E_d}{2E_o^3\left(E_o^2 - E_g^2\right)} \ln\left(\frac{2E_o^2 - E_g^2 - (\hbar\omega)^2}{E_g^2 - (\hbar\omega)^2}\right) \quad (1)$$

where n is the real refractive index, $\hbar\omega$ is the photon energy, E_g is the band gap at the gamma point, E_d is the dispersion energy and E_o is the oscillator energy that is related to the aluminium fraction, x, by the following equations from [12]

$$E_g = 1.89 + 0.67x \quad (2)$$

$$E_o = 4.17 + 0.49x \quad (3)$$

$$E_d = 35.79 - 1.16x \quad (4)$$

Owing to the thinness of the quantum wells, the optical mode was not very sensitive to the value of refractive index used for GaInP. We used a value of 3.57 for the real refractive index, corresponding to the highest real value we could calculate below the band edge. This value agreed with measurements by Moser *et al.* who measured the refractive indices of AlGaInP for aluminium (Al) fractions of 0, 0.33 and 0.66 [13] and Ferrini *et al.* [14]. We neglected any imaginary parts corresponding to gain or absorption at the lasing energy. The resulting calculated far-field intensity as a function of angle was directly compared with measured far-fields of lasers fabricated from grown wafers, recalculating far-field profiles for different lasing wavelengths if necessary.

To ensure comparison of model and experiment under the same conditions, at room temperature, the lasers were operated close to threshold and pulsed to avoid self-heating. The active region temperature of a laser operated CW will inevitably rise to a certain extent, depending on cooling arrangements. If CW or uncooled high-temperature operation is required the calculations would need to take into account the change in band gap and refractive index with temperature.

The temperature dependence of the band gap can be calculated using the formula of Varshni [15], for example,

doi: 10.1049/iet-opt.2014.0093

or, for a better fit over a wider temperature range an expression by O'Donnell and Chen [16] with fits to experimental data for (Al)GaInP by Smowton and Blood [17]. Calculations of the temperature dependence of the refractive index of semiconductors, mainly binaries, have been made by various workers [18–22]. Specific attention was paid to the (Al)GaInP system by Meney *et al.* [23] who extended the refractive index results of Moser *et al.* [13] over a range of temperatures. Our calculations indicated the thermal expansion of layers in a slab waveguide had a negligible effect.

From the resulting near-field and far-field profiles obtained, we calculated the optical confinement factors and the full-width-half-maximum (FWHM) and $1/e^2$ far-field widths. The confinement factor (Γ), defined as the spatial overlap of the gain producing quantum well with the optical mode intensity, was calculated from the near-field intensity profile, again treating the waveguide as a 1D slab with uniform profiles along the length of the device. Since threshold occurs when the modal gain ($G = \Gamma g$, where g is material gain) is equal to the sum of the optical losses a higher confinement factor results in a lower threshold current. Although the wells are placed close together at the centre of the main part of the optical mode each has a slightly different confinement factor. For ease of comparing structures, the average confinement factor (mean of the confinement factors over the three quantum wells) is used.

A portion of the mode is also confined in the ME layers. This must not interfere with the useful central portion of the beam and so is ideally small (and therefore not containing a large fraction of the optical power) and well separated from the central part.

We investigated the effect of varying the width and spacing of the ME layer (The core remained unchanged.). We varied the ME layer width from 210 to 460 nm and spacing from 200 to 900 nm over a wavelength range of 635–665 nm, calculating the FWHM and $1/e^2$ far-field divergence.

Throughout the modelling, we assumed the layer thicknesses and compositions remained the same in the core, and that changes in the cladding layers, including the ME layers, took place uniformly throughout both p and n claddings.

After modelling the designs, we selected two for growth by a commercial vendor: a narrow far-field design with an ME layer width of 250 nm and a spacing of 550 nm (Design A), and a very narrow far-field design with an ME layer width of 320 nm at a spacing of 750 nm (Design B). The core and active region remained the same throughout. Design A was grown three times over a period of about a year to investigate the stability of the far-field divergence with respect to manufacturing tolerances, Design B was grown once. As an illustration of the modelling process, the variation of confinement and divergence about these width and spacing values is shown in Fig. 2. Moreover, shown are the results for an asymmetric structure with an ME layer in the n-cladding only. The variation of the average confinement factor over the three quantum wells is shown in the top two sub-figures. In the left-hand figure, the spacing of the ME layer is held constant at 750 nm, as in Design B, and the thickness of the layer is varied from 250 to 370 nm. The confinement factor remains relatively high until a thickness of 320 nm and then starts to decrease rapidly: such a combination of values should be avoided in a design where reproducibility is required. For example, a design value of 15°, indicated by the grey horizontal dotted line in the bottom left sub-figure requires an ME width of 310 nm for a symmetric design, for which the confinement factor remains high. For an asymmetric design, the ME width would have to be 340 nm, moving the design into a region of rapidly varying confinement factor and greater sensitivity to growth

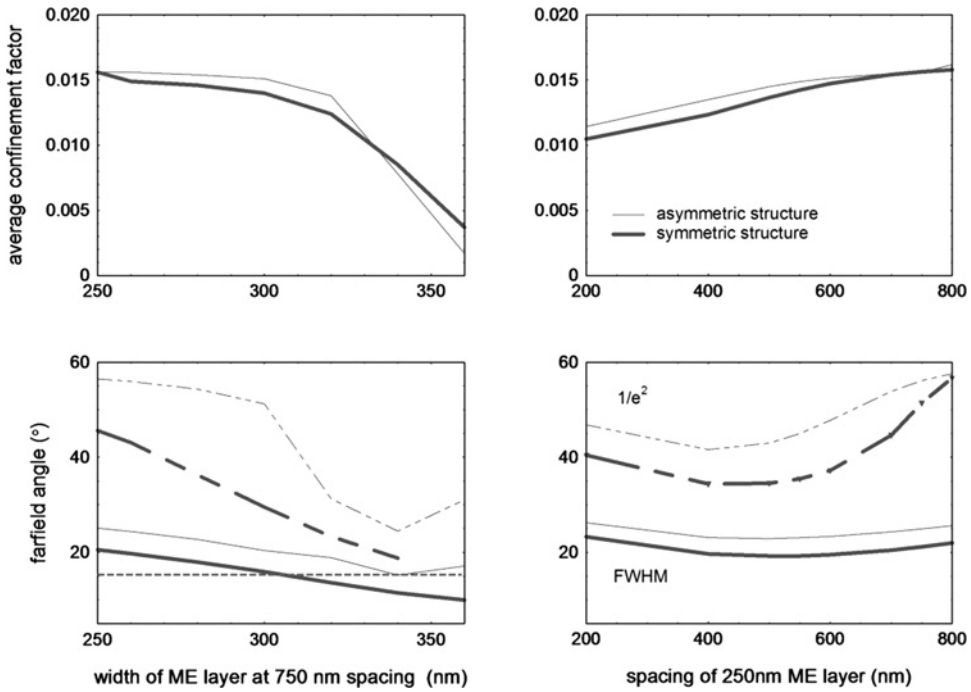

Fig. 2 *Structure design*

The variation of the average confinement factor (top figures) and the vertical far-field divergence (bottom figures) as the ME layer thickness (left) and spacing (right) are varied. Bold lines denote a symmetric structure and thin lines an asymmetric structure. FWHM far-fields are given as solid lines and $1/e^2$ far-fields as dashed lines. The horizontal dotted line in the bottom left sub-figure illustrates some disadvantages of using an asymmetric design to achieve a far-field of 15°: extra ME layer width is required and reduced confinement factor is obtained.

doi: 10.1049/iet-opt.2014.0093

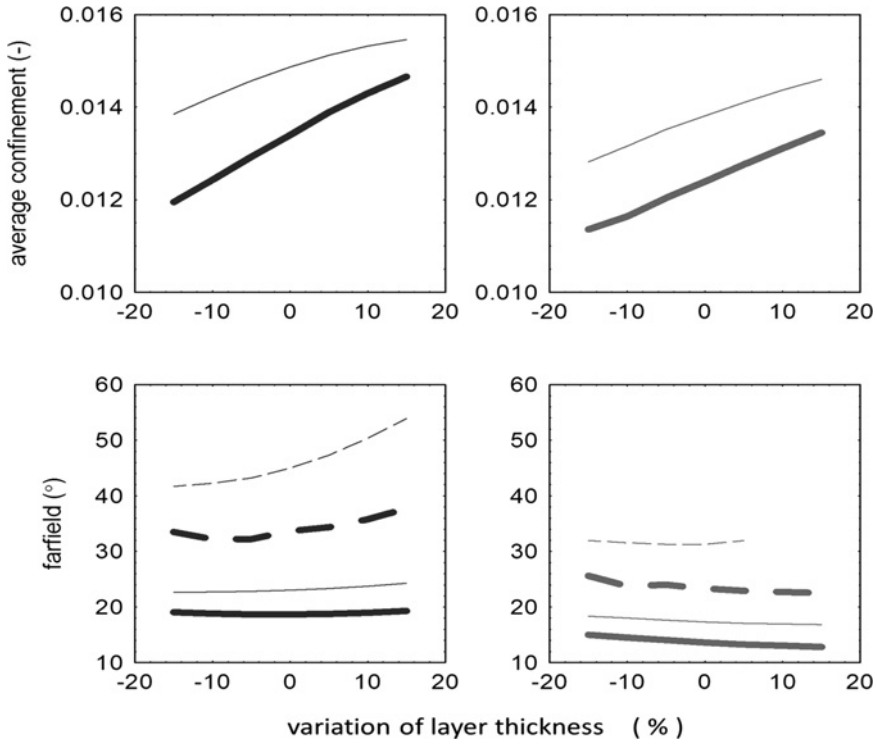

Fig. 3 *Thickness variation during growth*

The variation of the average confinement factor (top figures) and the vertical far-field divergence (bottom figures) as a function of a uniform percentage change in width and spacing of the ME layers for Design A (left-side sub-figures) and Design B (right-side sub-figures). Bold lines denote a symmetric structure and thin lines an asymmetric structure. FWHM far-fields are given as solid lines and $1/e^2$ far-fields as dashed lines.

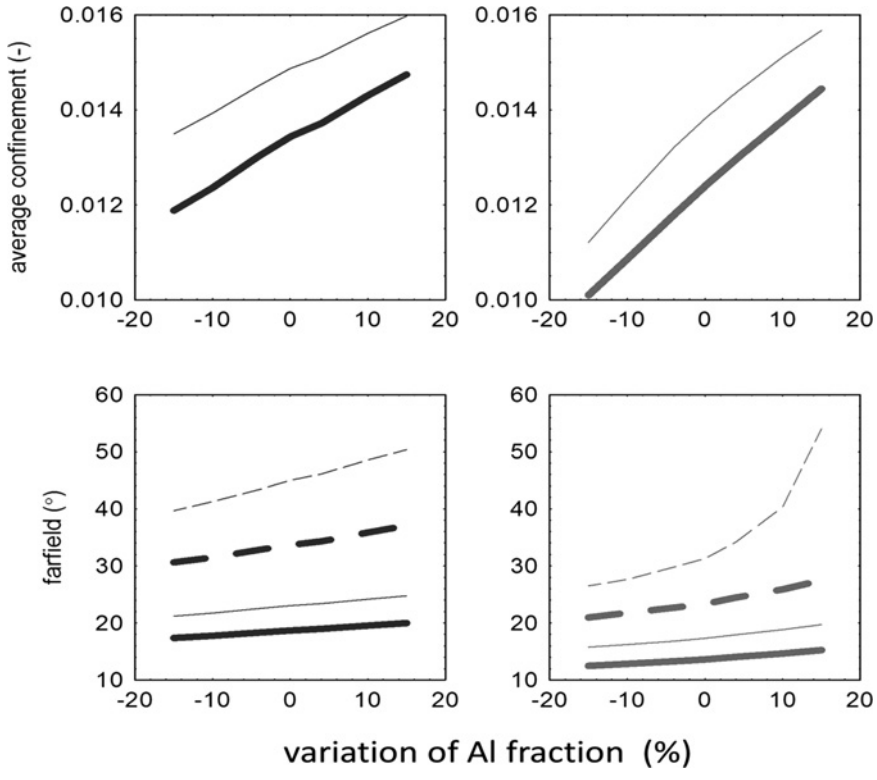

Fig. 4 *Composition variation during growth*

The variation of the average confinement factor (top figures) and the vertical far-field divergence (bottom figures) as the aluminium content is varied by up to 15% of its specified value uniformly in all cladding layers for Design A (left-side sub-figures) and Design B (right-side sub-figures). Bold lines denote a symmetric structure and thin lines an asymmetric structure. FWHM far-fields are given as solid lines and $1/e^2$ far-fields as dashed lines.

doi: 10.1049/iet-opt.2014.0093

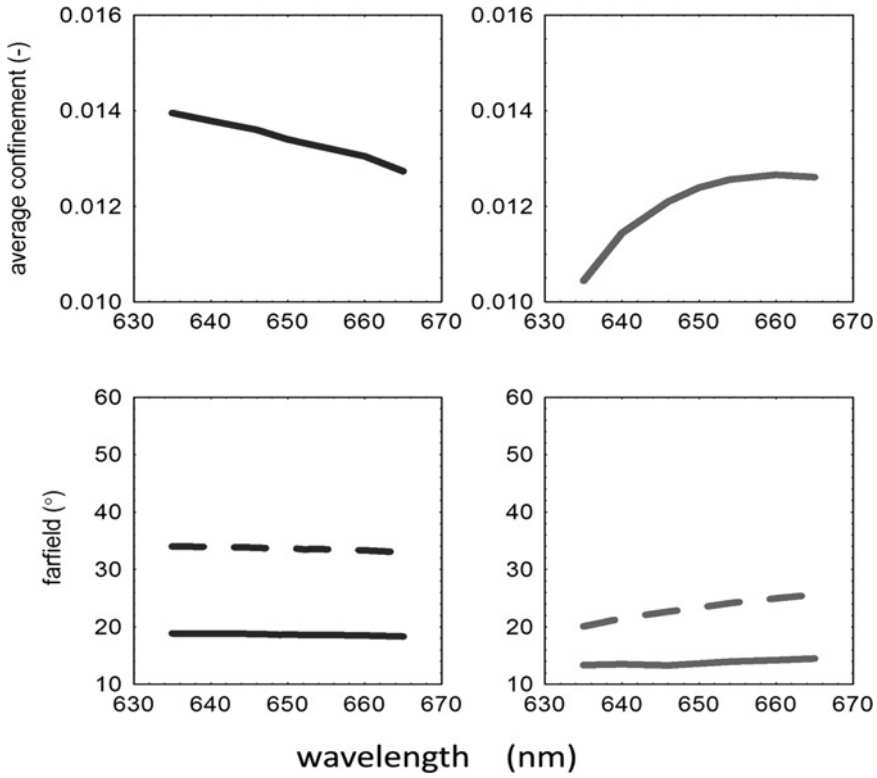

Fig. 5 *Emission wavelength variation during growth*

The variation of the average confinement factor (top figures) and the vertical far-field divergence (bottom figures) as the wavelength is varied (with refractive index change as a function of wavelength taken into account) for Design A (left-side sub-figures) and Design B (right-side sub-figures). FWHM far-fields are given as solid lines and $1/e^2$ far-fields as dashed lines.

conditions. The predicted FWHM far-field for Design B with two symmetrically placed 320 nm wide ME layers is 13.6°, this could not be achieved at all with an asymmetric design as multiple side lobes appear in the far-field beyond 340 nm. The symmetric design also has the advantage of a slower rate of variation of the confinement factor as the thickness of the ME layer varies, which has implications for the stability of the design in growth.

Of importance in the manufacturing process is the stability of the design to unintentional variations in layer thickness or composition. For the designs selected for growth, we modelled the effect of the change in thicknesses (Fig. 3) or composition of the AlGaInP cladding layers (Fig. 4). We also modelled the effect of a wavelength change (Fig. 5), including change in refractive index as a function of wavelength [12], since a wavelength change could be induced by thickness or composition induced well depth variation in the active region or variation in material quality or losses, for example. The core and active region thicknesses and compositions were held constant. Manufacturers' epitaxial growth tolerances for MOCVD are typically ±10% for layer thickness and ±3% for composition.

The values of the confinement factor calculated for Design A (with an ME layer on both sides) subject to manufacturing tolerance vary by ±6.5% as the layer thickness varies by ±10%. Those for Design B show a smaller variation. The far-field change is of the order of a degree, which is a small fraction of that of Design A and about 5% for Design B. The far-field divergences are more sensitive to growth changes in the asymmetric structures than symmetric, whereas the confinement factors are less sensitive. The changes, in general, are non-monotonic and modelling involves finding regions with slow rates of change.

The changes induced by a fractional change in aluminium content are of a similar magnitude to the changes because of variations in layer thickness by the same percentage. However, the far-field changes in the same sense for both designs (a decrease in aluminium content produces a narrower far-field), whereas a layer thickness increase produced a far-field increase in Design A, but a decrease in Design B.

We used a smaller wavelength range as a fraction of the design wavelength since large variations in wavelength would not be tolerable in practical applications. The range of lasing wavelengths observed for these devices lie well within this range.

We now examine the application of these ideas in practice and present the results of detailed measurements on three different growths, using standard manufacturing practice, of Design A, over a period of a year, and one growth of Design B.

3 Measurements on manufactured wafers

The four manufactured wafers were processed at the time of receipt into 50 µm oxide isolated stripe lasers and segmented contact test structures for spectral absorption measurements. A summary of measured values is given in Table 1. The lasers were cleaved into lengths between 1 and 0.32 mm. A repeat processing of the first wafer was also undertaken. All devices were mounted using conductive epoxy n-side down onto copper heat-sinks with a gold wire contact to the stripe, with facets as-cleaved. The lasers were operated pulsed throughout (600 ns pulses at 1 kHz) to ensure no self-heating. Far-field divergences (Fig. 6) were measured with the laser placed on a rotating table and the intensity measured directly (in arbitrary units)

doi: 10.1049/iet-opt.2014.0093

Table 1 Laser parameters measured values of room temperature threshold current and predicted and measured values of far-field widths for 50 μm broad area oxide-isolated stripe lasers fabricated from three growths of Design A and one growth of Design B

Design	A (growth 1)	A (growth 2)	A (growth 3)	B
ME layers				
Width, μm	0.25	–	–	0.32
Spacing, μm	0.55	–	–	0.75
Far-fields, °				
predicted FWHM	18.7	–	–	13.6
measured FWHM	17.5 ± 0.4	17.5 ± 0.2	17.2 ± 0.2	12.7 ± 0.1
predicted $1/e^2$	33.7			23.3
measured $1/e^2$	28.9			20.2
Lasing wavelengths, nm				
0.32 mm laser	651	654	654	652
1 mm laser	657	659	656	656
Room temperature threshold current, mA				
0.32 mm laser	243	171	235	221
1 mm laser	442	405	578	459

as a function of angle, rather than using a translating slit with a stationary sample. This was necessary to obtain good data for the low intensity side lobes. Far-fields were measured for 1 and 0.45 mm lasers at 1.2× threshold current. We found no significant difference between the two lengths and therefore gave the FWHM far-field width (Table 1) as a mean over eight lasers (four of each length) with the average deviation from the mean as the error. The slight increase in intensity at large angles on the left-hand side of the far-field for Design B was because of light from the rear facet reflected from the transistor header on which the heat-sink was mounted. This was prevented with matt black paint for the far-field measurements on multiple lasers. We also fabricated Design A into ridge lasers producing a round spot. Threshold current densities were determined as a function of temperature (Fig. 7). Also shown are absorption edges and lasing wavelengths (Fig. 8).

All structures had modal scattering loss of about 8 cm^{-1}, measured using the segmented contact method [24].

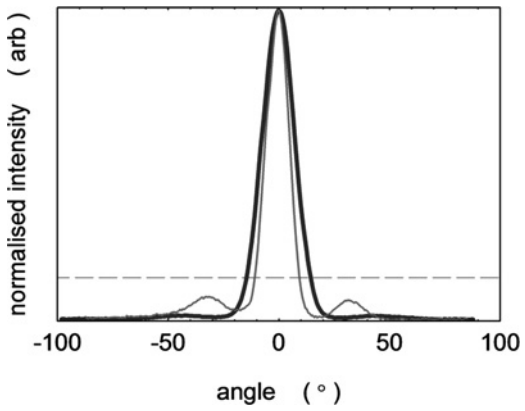

Fig. 6 *Laser far-field for the first growth of Design A showing a broader far-field and little evidence of side lobes (thick curve) and Design B with a narrower far-field, but evidence of side lobes (thin curve). The data have been normalised. The dashed line indicates $1/e^2$ of the peak value*

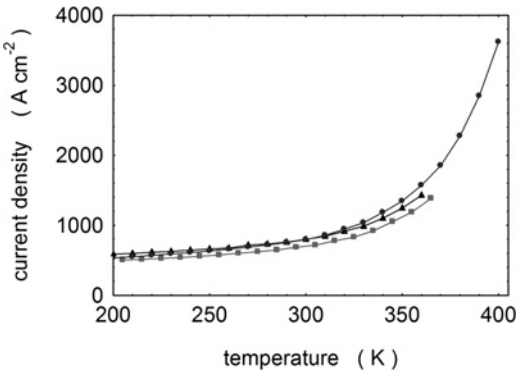

Fig. 7 *Laser threshold current density for 1 mm lasers fabricated from Design A (50 μm oxide isolate stripe, p-up with as-cleaved facets): first growth (circles), second growth (squares) and third growth (triangles)*

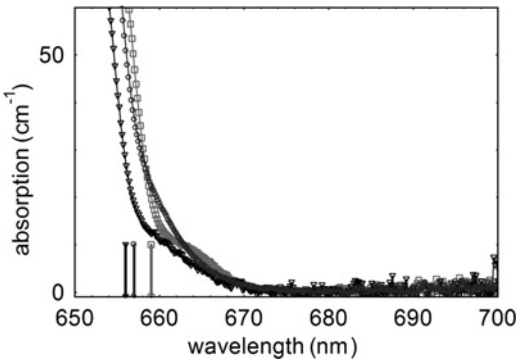

Fig. 8 *Absorption curves for the repeated growths of Design A, showing lasing wavelengths for 1 mm lasers: first growth (circles), second growth (squares) and third growth (triangles)*

We measured the power density at the facet for the narrow far-field design which achieved 14 (±2) $MWcm^{-2}$ at catastrophic optical damage [25]. The calculated spot size for this structure is 0.37 μm.

4 Discussion

The measured FWHM far-field widths are about 6% lower and the $1/e^2$ about 13% lower than the predicted values in both Design A and Design B. The consistency of the measured far-fields for all three growths of Design A (to within 0.3° FWHM) suggests good consistency in the growth. A change in Al fraction is the only variation that would cause the far-fields of both of the designs to change in the same sense. A reduction in the Al fractions of all cladding layers of about 13% would account for the changes in far-field; however, the good consistency means the growth could be adjusted to achieve the required far-field every time.

This design focuses on applications where a narrow far-field is highly desirable with a medium power output. This design could be extended to the 630 nm by a suitable choice of quantum well composition and strain.

5 Conclusions

In our wafers we found good consistent values of the FWHM far-field between growths of Design A over a period of a year, with a narrow FWHM vertical far-field divergence of 17°, and

doi: 10.1049/iet-opt.2014.0093

just under 13° for Design B. The modelling suggested good stability in the designs with respect to unintentional variations in layer thickness and composition during growth and this was borne out in the measured far-fields. Modelling predicted a slightly wider far-field than those measured and suggested the growth achieved a slightly lower aluminium fraction than specified, but a high degree of control. We have demonstrated a useful, reproducible design, adding to the range of versatile semiconductor lasers available for every application.

6 Acknowledgment

We acknowledge financial support from ESPRC grant no. EP/L005409/1.

7 References

1 Crump, P., Knigge, S., Maaβdorf, A., *et al*.: 'Low-loss, smile-insensitive external frequency-stabilization of high power diode lasers enabled by vertical designs with extremely low divergence angle and high efficiency'. *Proc. of SPIE*, 2013, **8605**, pp. 86050T-1–86050T-12

2 Paschke, K., Fiebig, C., Blume, G., *et al*.: 'Miniaturized highly brilliant diode laser modules for future display applications', *Opt. Rev.*, 2014, **21**, pp. 75–78

3 Pietrzak, A., Crump, P., Wenzel, H., Erbert, G., Bugge, F., Tränkle, G.: 'Combination of low-index quantum barrier and super large optical cavity designs for ultranarrow vertical far-fields from high power broad-area lasers', *IEEE J. Sel. Top. Quantum Electron.*, 2011, **17**, (6), pp. 1715–1722

4 Maximov, M., Shernyakov, Y.M., Novikov, I.I., *et al*.: 'High-power low-beam divergence edge-emitting semiconductor lasers with 1- and 2-D photonic bandgap crystal waveguide', *IEEE J. Sel. Top. Quantum Electron.*, 2008, **14**, (4), pp. 1113–1122, and references therein

5 Malag, A., Jasik, A., Teodorczyk, M., Jagoda, A., Kozłowska, A.: 'High-power low vertical beam divergence 800-nm-band double-barrier-SCH GaAsP–(AlGa) as laser diodes', *IEEE Photonics Technol. Lett.*, 2006, **18**, (15), pp. 1582–1584

6 Elliott, S.N., Smowton, P.M., Berry, G.: 'Optimisation of high power AlGaInP laser diodes for optical storage applications', *IEE Proc., Optoelectron.*, 2006, **153**, (6), pp. 321–325

7 Qiu, B., McDougall, S.D., Liu, X., Bacchin, G., Marsh, J.H.: 'Design and fabrication of low beam divergence and high kink-free power lasers', *IEEE J. Quantum Electron.*, 2005, **41**, (9), pp. 1124–1130

8 Chen, Y.C., Waters, R.G., Dalby, R.J.: 'Single quantum well laser with vertically integrated passive waveguides', *Appl. Phys. Lett*, 1990, **56**, (15), pp. 1409–1411

9 Smowton, P.M., Lewis, G.M., Blood, P., Chow, W.W.: 'Optimization of 635 nm tensile strained GaInP laser diodes', *IEEE J. Sel. Top. Quantum Electron.*, 2003, **8**, (5), pp. 1246–1251

10 Wemple, S.H., DiDomenico, M. Jr.: 'Behaviour of the electronic dielectric constant in covalent and ionic materials', *Phys. Rev. B*, 1971, **3**, (4), pp. 1338–1351

11 Afromowitz, M.A.: 'Refractive index of $Ga_{1-x}Al_xAs$', *Solid State Commun.*, 1974, **15**, pp. 59–63

12 Kaneko, Y., Kishino, K.: 'Refractive indices measurement of $(GaInP)_m/(AlInP)_n$ quasi-quaternaries and GaInP/AlInP multiple quantum wells', *J. Appl. Phys.*, 1994, **76**, (3), pp. 1809–1818

13 Moser, M., Winterhoff, R., Geng, C., Queisser, I., Scholz, F., Dörnen, A.: 'Refractive index of $(Al_xGa_{1-x})_{0.5}In_{0.5}P$ grown by metalorganic vapour phase epitaxy', *Appl. Phys. Lett.*, 1994, **64**, (2), pp. 235–237

14 Ferrini, R., Guizzetti, G., Patrini, M., Parisini, A., Tarricone, L., Valenti, B.: 'Optical functions of In GaP/GaAs epitaxial layers from 0.01 to 5.5 eV', *Eur. Phys. J. B*, 2002, **27**, pp. 449–458

15 Varshni, Y.P.: 'Temperature dependence of the energy gap in semiconductors', *Physica*, 1967, **34**, pp. 149–154

16 O'Donnell, K.P., Chen, X.: 'Temperature dependence of semiconductor band gaps', *Appl. Phys. Lett.*, 1991, **58**, (25), pp. 2924–2926

17 Smowton, P.M., Blood, P.: 'Visible emitting (AlGa)InP laser diodes', in Manasreh, M.O. (Ed.): 'Strained-layer quantum wells and their applications' (Gordon and Breach, Amsterdam, 1997), pp. 431–487

18 Yu, P.Y., Cardona, M.: 'Temperature coefficient of the refractive index of diamond- and zinc-blende-type semiconductors', *Phys. Rev. B*, 1970, **2**, (8), pp. 3193–3197

19 Wemple, S.H.: 'Refractive-index behaviour of amorphous semiconductors and glasses', *1973, Phys. Rev. B*, 1970, **7**, (8), pp. 3767–3777

20 Bogdanov, V.B., Pikhtin, A.N., Prokopenko, V.T., Yas'kov, A.D.: 'Temperature dependence of the refractive indices in semiconductors', *J. Appl. Spectrosc.*, 1987, **51**, pp. 1097–1100

21 Hervé, P.J.L., Vandamme, L.K.J.: 'Empirical temperature dependence of the refractive index of semiconductors', *J. Appl. Phys.*, 1995, **77**, (10), pp. 5476–5477

22 Gehrsitz, S., Reinhart, F.K., Gourgon, C., Herres, N., Vonlanthen, A., Sigg, H.: 'The refractive index of $Al_xGa_{1-x}As$ below the band gap: accurate determination and empirical modelling', *J. Appl. Phys.*, 2000, **87**, (11), pp. 7825–7837

23 Meney, A.T., Prins, A.D., Phillips, A.F., *et al*.: 'Determination of the band structure of disordered AlGaInP and its influence on visible-laser characteristics', *IEEE J. Sel. Top. Quantum Electron.*, 1995, **1**, (2), pp. 697–706

24 Blood, P., Lewis, G.M., Smowton, P.M., Summers, H., Thomson, J., Lutti, J.: 'Characterization of semiconductor laser gain media by the segmented contact method', *IEEE J. Sel. Top. Quantum Electron.*, 2003, **9**, (5), pp. 1275–1282

25 Elliott, S.N.: 'High power semiconductor lasers', PhD thesis, Cardiff University, 2010

doi: 10.1049/iet-opt.2014.0093